Species-specific wiring for direction selectivity in the mammalian retina

Huayu Ding[1], **Robert G. Smith**[2], **Alon Poleg-Polsky**[1], **Jeffrey S. Diamond**[1], and **Kevin L. Briggman**[3,4]

[1]Synaptic Physiology Section, National Institute of Neurological Disorders and Stroke, Bethesda, MD

[2]Department of Neuroscience, University of Pennsylvania, Philadelphia, PA

[3]Department of Biomedical Optics, Max Planck Institute for Medical Research, Heidelberg, Germany

[4]Circuit Dynamics and Connectivity Unit, National Institute of Neurological Disorders and Stroke, Bethesda, MD

Summary

Directionally tuned signaling in starburst amacrine cell (SAC) dendrites lies at the heart of the direction selective (DS) circuit in the mammalian retina. The relative contributions of intrinsic cellular properties and network connectivity to SAC DS remain unclear. We present a detailed connectomic reconstruction of SAC circuitry in mouse retina and describe previously unknown features of synapse distributions along SAC dendrites: 1) input and output synapses are segregated, with inputs restricted to proximal dendrites; 2) the distribution of inhibitory inputs is fundamentally different from that observed in rabbit retina. An anatomically constrained SAC network model suggests that SAC-SAC wiring differences between mouse and rabbit retina underlie distinct contributions of synaptic inhibition to velocity and contrast tuning and receptive field structure. In particular, the model indicates that mouse connectivity enables SACs to encode lower linear velocities that account for smaller eye diameter, thereby conserving angular velocity tuning. These predictions are confirmed with calcium imaging of mouse SAC dendrites in response to directional stimuli.

Introduction

A thorough understanding of a neuronal circuit requires a detailed anatomical wiring diagram that includes the synaptic connectivity among the component neurons. Even ostensibly subtle connectivity differences during development or between species could

underlie significant changes in circuit behavior. This is exemplified in the direction selectivity (DS) circuit in the mammalian retina, a model neural network that engages just a few well-characterized cell types to compute salient visual information. The detailed synaptic connectivity among these neurons, however, and circuitry differences between species, has not been completely described.

Direction-selective ganglion cells (DSGCs) respond strongly to visual motion in one (preferred) direction but only weakly to motion in the opposite (null) direction[1]. Bipolar cells (BCs) provide excitatory synaptic inputs to DSGCs and to densely arrayed SACs, which then inhibit DSGCs (Figure 1a)[2,3]. SAC dendrites oriented asymmetrically to a DSGC provide feedforward inhibitory input that establishes the DSGC's directional tuning[4,5]. SAC dendrites are themselves DS and release GABA from synaptic terminals at their tips preferentially in response to outward (centrifugal, CF) compared to inward (centripetal, CP) motion relative to their soma[6–8]. Several mechanisms contribute to DS within individual SAC dendrites, but their relative importance is unclear. Proposed intrinsic mechanisms include dendritic morphology[9], non-uniform chloride homeostasis[10], and active membrane conductances[6,11]. SAC DS may also rely on network interactions, such as spatially offset synaptic inputs from particular BC types[12] and reciprocal inhibition between neighboring SACs[8,13–16].

Most anatomical analyses of SAC microcircuitry have been performed in rabbit retina. Sparse electron microscopy reconstructions in rabbit indicated that excitatory and inhibitory synaptic inputs occur along the entire length of SAC dendrites, whereas inhibitory synaptic outputs arise on the distal third[2]. We explored SAC connectivity in mouse retina using serial block-face scanning electron microscopy (SBEM)[17]. We discovered a previously unknown asymmetric distribution of inhibitory and excitatory input synapses onto ON and OFF mouse SAC dendrites that is fundamentally different from the connectivity in rabbit retina. We developed an anatomically constrained network model of mouse SAC connectivity that predicts novel roles for synaptic inhibition in velocity and contrast tuning and receptive field structure in SACs. Finally, we confirmed these predictions by recording directionally tuned responses in mouse SAC dendrites. Our results indicate that the SAC network has adapted to meet specific demands imposed by the mouse visual system.

Results

Synaptic inputs are spatially offset

We annotated an ON-OFF DSGC within a conventionally stained SBEM volume ($50 \times 210 \times 260 \ \mu m^3$) from an adult mouse retina (Extended Data Figure 1a,b). Neurites forming conventional (inhibitory) synapses (Figure 1b) onto this cell were back-traced to identify four SACs (2 ON, 2 OFF) located centrally in the data volume (Figure 1c–e, Extended Data Figure 1c–e). Each SAC's morphology was fully traced within the data volume and the locations of input and output synapses were annotated. As expected, output synapses arose along the distal third of SAC dendritic trees (Figure 1f,g). Ribbon-type input synapses (Figure 1b) from BCs were distributed primarily along the proximal two-thirds of dendrites (Figure 1f,g). Conventional synapses from amacrine cells (Figure 1b) were restricted to the initial third of the dendritic trees (Figure 1f,g). This proximal location of amacrine cell

inputs differs from previous reports in rabbit retina that SACs receive reciprocal SAC inputs along their distal dendrites (Extended Data Figure 1f)[2,8,16,18], indicating that SAC connectivity is fundamentally different in mice and rabbits. Next, we identified cells presynaptic to the SACs.

BC and AC types presynaptic to SACs

Recent analysis of contact area shared between different OFF BC types and OFF SACs suggested a 'space-time wiring' presynaptic delay model that supports SAC DS[12]. In this model, different BC types exhibit distinct release kinetics[19–21], and sustained BCs (e.g., BC2) provide input more proximally on SAC dendrites than do transient BCs (e.g., BC3a). Because the present dataset allowed us to positively identify synapses, we classified BC types providing input to ON and OFF SACs (Figure 2); we noted several differences compared to the contact-based analysis[12].

We found synapses onto the OFF SACs from all OFF BC types (BC1, BC2, BC3a, BC3b, and BC4; Figure 2a,b, Extended Data Figure 2) with most input from BC1, BC2, and BC3a (Figure 2a,b). BC1 and BC3a exhibited segregated radial distributions, potentially supporting a presynaptic space-time wiring model, but BC2 overlapped with both; this overlap, regardless of BC2 response kinetics, would presumably diminish DS generated in such a model. Space-time wiring may still support DS in OFF SACs, pending characterization of type-specific OFF BC response kinetics. Our data suggest that SAC dendrites may simply sample from the available BCs at a particular IPL depth (Figure 2c), regardless of BC release characteristics.

If space-time wiring were essential for SAC DS, one would expect a similar connectivity pattern for ON SACs. BC inputs to the ON SACs clustered into four subtypes, corresponding to BC7 and three BC5 subtypes (BC5o, BC5t, BC5i)[22] (Figures 2d,e, Extended Data Figure 3). We found that BC7s primarily contacted proximal dendrites, whereas BC5 inputs, collectively, were distributed more distally (Figure 2d,e). Synapses' radial location correlated with their IPL depth (Figure 2f). Segregated BC inputs to ON SACs could support a space-time DS mechanism, although BC7s (which we show provide proximal inputs) exhibit transient light responses[23], counter to the model's requirements.

Next, we analyzed the sources of amacrine cell synapses onto the ON and OFF SACs (Figure 3a,b, Extended Data Figure 4). Most inputs originated from neighboring SACs, identified by their distinctive branching pattern and tight co-stratification with the postsynaptic SACs (Figure 3a, Extended Data Figure 4a,b). There was no directional preference in the absolute orientations of presynaptic SAC dendrites. Previous studies hypothesized that SAC DS could be enhanced if opposing ('anti-parallel') SAC dendrites preferentially made reciprocal connections[8,13]. To test this idea, we measured the relative angle between connected presynaptic and postsynaptic dendrites (Figure 3c, Extended Data Figure 5a,b). The distributions of relative angles for both the ON and OFF SACs were significantly skewed toward anti-parallel (180°) wiring (Kolmogorov-Smirnov test, p = 2×10^{-53} ; Figure 3c). We considered whether presynaptic SAC dendrites selectively connect to opposing dendrites or whether the relative angle distribution simply reflects the inter-soma spacing between SACs. We annotated locations where the distal third of presynaptic SAC

dendrites passed within 1 μm of the postsynaptic SACs and measured the relative angles between dendrites at each proximity. The proximity-based relative angle distribution was not statistically significantly different from the distribution based on actual synaptic connectivity (Extended Data Figure 5c, Kolmogorov-Smirnov test, p = 0.18), indicating that the wiring arises primarily from the geometric arrangement of connected SACs. Relative angle was not correlated to the radial distance of each synapse from the respective postsynaptic SAC soma (Extended Data Figure 5d).

Not all inhibitory inputs came from neighboring SACs. We annotated several apparent wide-field amacrine cells (WACs) that contributed synapses specifically onto the most proximal dendrites of ON and OFF SACs (Extended Data Figure 4c,d). WACs did not co-stratify with SACs, but rather stratified close to the inner nuclear and ganglion cell (GC) layers, in contrast to a different population targeting BC axon terminals presynaptic to DSGCs[24]. We also found a few synapses from narrow-field amacrine cells (NACs), mostly onto ON SACs (Extended Data Figure 4e)[25]. Therefore, although most proximal amacrine inputs originate from neighboring SACs, additional inputs may selectively inhibit perisomatic compartments.

We also quantified the number and types of postsynaptic targets of ON and OFF SAC branches terminating near the center of the data volume (Extended Data Figure 6). We traced postsynaptic cells until they could be identified unambiguously as a GC, SAC, WAC, or BC. Synapses were formed primarily onto GCs and SACs, with few outputs onto BCs, consistent with findings that BC terminals are not directionally tuned[26–28]. ON SACs devoted a higher fraction of outputs to GCs than did OFF SACs, possibly because ON SACs provide inputs to both ON-OFF DSGCs and ON DSGCs.

Proximal excitation enhances SAC DS

Our anatomical data indicate that BC inputs are restricted to the proximal two-thirds of SAC dendrites and SAC inputs are restricted to the proximal third. Next, we combined computational modeling and physiological imaging to examine how this connectivity pattern affects response properties of SAC dendrites.

We based a single-cell SAC model on an existing passive model[9] and incorporated measured dendritic diameters and active conductances along the dendrites such that the dendrites and soma both preferred CF motion (Extended Data Figure 7, Extended Data Table 1)[6]. We then constructed a network model comprising one central SAC and 6 surrounding SACs (Figure 4a). SAC-SAC synapses were formed when a presynaptic dendrite came within a criterion distance of a postsynaptic cell. The inter-soma distance (145 μm) was set to reproduce the relative angle distributions observed anatomically (Extended Data Figure 5) and the radial distribution of inhibitory synapses (Figure 4b, upper panel). We then measured the direction selectivity index (DSI, see Methods) at a distal dendritic location (ROI*, Figure 4d) on the central SAC (Figure 4a, boxed region).

In response to moving bar stimuli, ROI* preferred CF motion compared to CP motion, as expected (Figure 4d). During CF motion, depolarization of the dendritic tips preceded inhibition from neighboring SACs. During CP motion, inhibition preceded excitation and limited depolarization of ROI*. We then modified the model to test whether the spatial

separation between excitatory inputs and SAC outputs is important for DS. When BC inputs were uniformly distributed along SAC dendrites, thereby overlapping with outputs, ROI* preferred CP over CF motion (Figure 4e). BC inputs on distal tips increased surround inhibition during CF motion and caused excitation to lead inhibition during CP motion, thereby reducing DS. This result suggests that restricting excitation to the proximal two-thirds of SAC dendrites establishes a temporal pattern of excitation and inhibition that enhances preference for CF motion.

Inhibition shapes velocity tuning

When we simulated rabbit-like connectivity by increasing the inter-soma distances (200 μm) to generate distal SAC-SAC contacts (Figure 4b, lower panel, 4c), the model still exhibited CF preference. The most obvious distinction between the mouse and rabbit eye is a five-fold difference in diameter (Extended Data Figure 8a)[29,30]. Consequently, a 1° visual angle subtends 30 μm on the mouse retina and 150 μm on the rabbit retina. Mouse and rabbit DSGCs respond to similar angular velocities[31,32] (Extended Data Figure 8c), suggesting that SACs in both species are also tuned to similar angular velocities.This translates to different linear velocities: 10°/s motion corresponds to 1500 μm/s across rabbit retina but just 300 μm/s across mouse retina (Extended Data Figure 8b).

Both the mouse and rabbit SAC models exhibited DS at linear velocities above 500 μm/s (Figure 4g). At lower velocities, however, DS in the rabbit model degraded because surround inhibition and central excitation did not overlap sufficiently in time to inhibit CP responses as strongly (Figure 4i). The reduced DS at lower velocities is consistent with velocity tuning measured in rabbit DSGCs (Extended Data Figure 8)[31]. By contrast, the mouse model remained DS down to 100 μm/s. The greater spatial overlap of synaptic inputs from neighboring SACs and BCs in mouse enabled inhibition to coincide with excitation at lower linear velocities during CP motion (Figure 4h). Increasing SAC inter-soma distances to 250 μm, generating tip-to-tip connectivity, further shifted the tuning curve to higher velocities (Figure 4g).

We tested the model's prediction by performing two-photon laser scanning microscopy[33] of dendritic calcium from mouse SACs filled with OGB1 in whole mount retinas[34] (Figure 4j). Bars of light were swept across SAC receptive fields in 8 equally spaced directions at linear velocities ranging from 30 – 2000 μm/s; DS was calculated from calcium transients measured at individual distal varicosities. As the model predicted, mouse SACs remained DS down to at least 100 μm/s (Figure 4k,l). These results suggest that SAC circuitry has adapted to conserve angular velocity tuning across species.

SAC-SAC inhibition expands contrast range

To encode naturalistic stimuli effectively, SACs must also remain DS over a wide contrast range[24,35], a feature predicted by our model (Figure 5a,b). Simulations suggested that broad contrast tuning requires SAC-SAC inhibition: at high contrasts, blocking inhibition dramatically reduced DS in simulated SACs due to saturation of postsynaptic responses to both CF and CP stimuli (Figure 5c).

We tested these predictions by imaging SAC dendritic responses to directional motion at different visual contrasts (Figure 5d–g). Consistent with the model, SACs remained DS over different contrast levels and blocking SAC-SAC inhibition with a GABA$_A$ receptor (GABA$_A$R) antagonist, SR95531 (25 μM), significantly reduced DS particularly in response to high contrast stimuli (Figure 5g).

Inhibition shapes SAC receptive fields

In rabbit retina most SAC-SAC connections occur between distal dendrites (Extended Data Figure 1f)[2]; consequently, DS for stimuli restricted to a SAC's central receptive field relies primarily upon intrinsic dendritic conductances rather than network inhibition[6,7]. In the mouse retina, we found that SACs receive SAC inputs exclusively on their proximal dendrites (Figure 1), suggesting that DS within the central receptive field may rely on inhibition from neighboring SACs.

We explored this first in our mouse network model using a radially expanding or contracting ('bulls-eye') stimulus previously described (Figure 6a,b)[6]. The model exhibited strong CF DS in response to the bulls-eye stimulus with inhibition intact, because proximal inhibitory synapses became activated by centrally restricted stimuli (Figure 6c). Removing inhibition reduced CF DS over a range of simulated contrasts (Figure 6c,d). We tested the model's prediction by imaging dendritic calcium signals evoked by bulls-eye stimuli restricted to the SAC dendritic arbor (Figure 6e). Blocking inhibition with SR95531 significantly reduced DS (Figure 6f,g), as the model predicted. SR95531 may also influence presynaptic inhibition of BC terminals, potentially disrupting BC type specific release kinetics. If this were the case, however, dendrite autonomous rabbit SAC DS should also be reduced by SR95531, contrary to previous reports[6,7].

Discussion

When reconstructing wiring diagrams, an important question is what level of detail is required to understand mechanistically how a neuronal circuit performs specific computations[36,37]. Our results indicate that seemingly subtle differences in connectivity – such as whether cells receive inputs on proximal versus distal dendrites – can substantially influence neural coding and circuit behavior. We found that segregating excitatory inputs from synaptic outputs along SAC dendrites helps establish strong CF DS in a network model of SAC connectivity (Figure 4e, also see[38]). More importantly, comparing wiring diagrams across species revealed a previously unrecognized connectivity difference in DS circuits of the mouse and rabbit retina (Figure 1, Extended Data Figure 1).

The two species exhibit comparable average SAC dendritic diameters and coverage factors[39–42], suggesting that mouse and rabbit SAC networks theoretically could have been wired similarly. We found instead that the locus of presynaptic inhibition on SACs alters the linear velocity tuning of SAC DS to compensate for eye size difference and conserve angular velocity tuning across the two species (Figure 4). Inhibition among SACs also extended their contrast tuning range (Figure 5): removing inhibition reduced SAC DS at high stimulus contrasts, potentially rendering postsynaptic DSGCs blind to directional motion. Proximal

inhibition also altered the receptive field structure of mouse SACs compared to previous reports of rabbit SACs (Figure 6)[6,7].

Our simulations effectively guided our physiological experiments, but they underepresented the extensive connectivity of SACs, which actually receive inputs from dozens of neighboring SACs (Figure 3). The model also neglects inhibitory inputs to SACs from WACs and NACs and detailed features of the presynaptic BC circuitry, important elements to incorporate in future simulations. Other visual stimulus features (e.g., size, shape, spatial frequency) also remain to be explored. Nevertheless, the present study exemplifies how connectomic mapping, computational modeling and cellular physiology complement each other to provide new insights into neuronal circuit computations.

Methods

No statistical methods were used to predetermine sample size. All n values refer to biological replicates.

EM tissue preparation

An adult wild-type (C57BL/6) mouse (P30) was anaesthetized with Isoflurane (Baxter) inhalation and killed by cervical dislocation. The eyes were enucleated and transferred to a dish containing carboxygenated room-temperature saline, in which the retinas were dissected. All procedures were approved by the local animal care committee and were in accordance with the law of animal experimentation issued by the German Federal Government. We used a commercially available saline (Biometra) that was supplemented with 0.5 mM l-glutamine and carboxygenated (95% O_2/5% CO_2). We hemisected the retina and mounted it on filter paper. The retina was fixed in a solution containing 0.1 M cacodylate buffer, 4% sucrose and 2% glutaraldehyde, pH 7.2 (Serva). The tissue was fixed for 2 h at room temperature and then rinsed in 0.1 M cacodylate buffer + 4% sucrose overnight. A 1×1 mm^2 region of the retina, approximately halfway between the optic disk and the peripheral edge of the retina, was then excised. The tissue was then stained in a solution containing 1% osmium tetroxide, 1.5% potassium ferrocyanide, and 0.15 M cacodylate buffer for 2 h at room temperature. The osmium stain was amplified with 1% thiocarbohydrazide (1 h at 50 °C), and 2% osmium tetroxide (1 h at room temperature). The tissue was then stained with 2% aqueous uranyl acetate for 12 h at room temperature and lead aspartate for 12 h at room temperature. The tissue was dehydrated through an ethanol series (70%, 90%, 100%), transferred to propylene oxide, infiltrated with 50%/50% propylene oxide/Epon Hard, and then 100% Epon Hard. The block was cured at 60 °C for 24 h.

SBEM acquisition

The retina (k0725) was cut out of the flat-embedding blocks and re-embedded in Epon Hard, on aluminium stubs for SBEM, with the retinal plane vertical. The samples were then trimmed to a block face of ~200 μm wide and ~400 μm long. The samples were imaged in a scanning electron microscope with a field-emission cathode (QuantaFEG 200, FEI Company). Back-scattered electrons were detected using a custom-designed detector based

on a special silicon diode (AXUV, International Radiation Detectors) combined with a custom-built current amplifier. The incident electron beam had an energy of 2.0 keV and a current of ~110 pA. Images were acquired with a pixel dwell time of 2.5 μs and size of 13.2 nm × 13.2 nm which corresponds to a dose of about 10 electrons per nm^2. Imaging was performed at high vacuum, with the sides of the block evaporation-coated with a 100–200 nm thick layer of gold. The electron microscope was equipped with a custom-made microtome designed by Winfried Denk that was previously used to collect retinal SBEM data[4,44]. The section thickness was set to 26 nm. 10112 consecutive block faces were imaged, resulting in aligned data volumes of 4992 × 16000 × 10112 voxels (1 × 5 mosaic of 3584 × 3094 images), corresponding to an approximate spatial volume of 50 × 210 × 260 μm^3. The edges of neighboring mosaic images overlapped by ~1 μm. The cutting quality degraded during the course of the experiment, meaning the images in the first half of the data volume (approximately the first 5000 slices) are of higher quality than the second half of the volume. Nevertheless, thin neurites could be manually annotated throughout the volume. The imaged region spanned the inner plexiform layer of the retina and included the ganglion cell layer and part of the inner nuclear layer. Cross-correlation-derived shift vectors between neighboring mosaic images and consecutive slices were used for a global least-squares fit across all shift vectors to align the data sets off-line to subpixel precision by Fourier shift-based interpolation. The data sets were then split into cubes (128 × 128 × 128 voxels) for viewing in KNOSSOS (www.knossostool.org).

Skeleton tracing and contact annotation

Skeletons were traced using KNOSSOS and consisted of nodes and connections between them. Nodes were placed approximately every 250 nm. Synapses were manually identified and annotated within Knossos. All analyses of skeletons were performed using Matlab (The Mathworks).

Modeling

We constructed models of an individual SAC and a network of 7 SACs using the simulation language Neuron-C[45]. We digitized a SAC morphology from a confocal stack of a labeled SAC, but included a multiplicative "diameter factor" set for each dendritic region based on the dendritic diameters measured from the EM reconstructions (Figure S7A). The SAC network was assembled with an algorithm that synaptically interconnected the SAC dendrites based on their location and orientation. Each SAC typically made a total of 120–250 inhibitory synapses onto its neighbors. The central SAC received about twice the number of inhibitory synapses as the surrounding SACs because of the "edge effect." Therefore, to achieve a balance between inhibition in the central SAC and its 6 surrounding SACs, we reduced the conductance of the surround → central inhibitory synapses by 50%. BCs were created in a semi-random pattern and were connected to SACs with ribbon synapses if they were within a criterion distance. Synapses were modeled as Ca^{2+}-driven neurotransmitter release that bound to a postsynaptic channel defined by a ligand-activated Markov sequential-state machine[45,46]. The excitatory conductances were typically set to 230 pS and inhibitory conductances were typically 80–160 pS. Membrane ion channels were defined by a voltage-gated Markov state machine and were placed at densities specified for each region of the cell. See Extended Data Table 1 for biophysical parameters.

The contrast of the stimulus presented to the SAC models was achieved by varying the strength of excitatory input from BCs. This was accomplished by voltage-clamping a presynaptic compartment that represented each BC according to the spatio-temporal pattern of the stimulus. The presynaptic holding potential in the BCs was just above the threshold for synaptic release, typically ~ –45 mV.

The synaptic connectivity of the SAC output synapses was set automatically by an algorithm based on the orientation of presynaptic and possible candidates for the postsynaptic dendrite. When the orientations of both dendrites were within a specific angular range, a synaptic connection was made. This synaptic placement depended on several other criteria, e.g. whether the presynaptic point fit within the allowable spacing and radial distribution on the presynaptic dendrite, and also whether the closest point on the postsynaptic dendrite was within a specified distance. The orientations were computed as the absolute angle from the prospective presynaptic point on the distal dendrite to the soma.

Direction selectivity indices were calculated based on the calcium concentration at a location along a central SAC dendrite using the following equation: DSI = (PD – ND)/PD, where PD is the response in the CF direction and ND is the response in the CP direction.

Models were run on an array of 3.2 GHz AMD Opteron CPUs interconnected by Gigabit ethernet, with a total of 220 CPU cores. Simulations of the 7-SAC model took 4 – 48 hours, depending on the model complexity and duration of simulated time. The simulations were run on the Mosix parallel distributed task system under the Linux operating system.

Physiological recordings: tissue and calcium-indicator loading

All physiological animal procedures were conducted in accordance with US National Institutes of Health guidelines, as approved by the National Institute of Neurological Disorders and Stroke Animal Care and Use Committee (ASP 1361). Both male and female adult (p30 – p60) ChAT-tdTomato mice were used in the experiments (Jackson Laboratory). The mice were anaesthetized with Isoflurane (Baxter) inhalation and killed by cervical dislocation. Retinas were isolated and all subsequent procedures were performed at room temperature in Ames media (Sigma) equilibrated with 95% O_2/5% CO_2. Sharp electrodes were pulled on a P-97 Micropipette Puller (Sutter) with a resistance of 100–150 MOhms. Iontophoresis of Oregon Green 488 BAPTA-1 (OGB1, Life Technologies) into single cells was achieved by applying the buzz function in MultiClamp 700B software at 50ms pulses (Molecular Devices) while the electrode filled with OGB1 (15mM in water) was on the cell membrane. Pipettes were withdrawn as soon as cell bodies began to fill, and cells were left to recover for 20–30 min prior to imaging. To block inhibition, the $GABA_A$ receptor antagonist SR95531 (25 μM, Tocris) was added to the extracellular medium.

Physiological recordings: two-photon microscopy

For two-photon imaging, we used a customized microscope (Sutter Movable Objective Microscope), controlled by ScanImage[47], equipped with through-the-objective light stimulation[34] and two detection channels for fluorescence imaging (green, BP 500–540, and red, BP 575–640; Chroma/Thorlabs). The excitation source was a mode-locked Ti/sapphire laser (Chameleon, Coherent) tuned to 920 nm. The microscope was used to simultaneously

visualize ChAT-tdTomato-labelled SACs for single cell targeting (red channel) and to monitor calcium activity reflected by OGB1 fluorescence changes (green channel). During functional imaging, the scan parameters were 256×100 pixels at 10 Hz frame rate. Scanning was triggered by the light stimulation. Field of view during acquisition was 80 μm × 80 μm.

Physiological recordings: light stimulation

Light stimulation was generated by custom-written code in Igor software (Wavemetrics) and 4D Workshop 4 IDE (4D Systems) to control an LCD mask in front of a collimated LED (405 nm, Thorlabs) with a bandpass filter (BP 405, Thorlabs). The stimuli were projected onto the retina through the objective lens (XLUMPlanFL 20× 0.95 NA water-immersion, Olympus). Stimulus contrast varied between 100 – 300%, with the 300% stimulus intensity at ~25×10^3 photons s^{-1} μm^{-2} on a background intensity of ~6×10^3 photons s^{-1} μm^{-2}. For the bar stimulus, the bar (400×400 μm) moved in one of eight evenly – spaced directions at a range of velocities between 0.03 – 1 mm s^{-1}. The bullseye stimulus was configured as previously described[6]. Each stimulus was repeated 3 – 5 times and responses were averaged.

Calcium-imaging data analysis

Image stacks were analyzed using custom Igor (Wavemetrics) functions. Image segmentation was performed by simple thresholding and ROIs are selected as varicosities along dendrites. Response to each stimulus was calculated as the average F/F during 1 sec after stimulus onset; baseline was determined by measuring the fluorescence prior to the stimulus. The responses were averaged across stimulus presentations. DSI was calculated by (PD – ND)/ND, where ND is the null (or CP) and PD is the preferred (or CF) response.

Statistical analyses

We included as much of the raw anatomy data as practical in the figures, including neuron and synapse distributions and spatial locations. The identities of neurons presynaptic to SACs were, by definition, blind to the annotator prior to skeletonization. No reconstructed neurons were excluded from the analysis. For comparing relative angle distributions, we used the non-parametric Kolmogorov-Smirnov test. For dendritic calcium experiments incorporating pharmacology, all measurements were paired (i.e., responses at a ROI are reported both before and after drug application). The number of recorded cells was selected to provide typically hundreds of ROIs for comparison and paired t-tests were used to assess statistical significance. All samples sizes and statistical test results are reported in the figure legends. Statistical tests were performed in Matlab or Graphpad.

Code availability

The Neuron-C simulation language that generated the models described above is available at: ftp://retina.anatomy.upenn.edu/pub/rob/nc.tgz. Included in this distribution is the realistic SAC morphology, the "retsim" retinal circuit simulator that generated the models, and the "rsbac_stim_plots_vel" script that ran multiple model jobs in parallel.
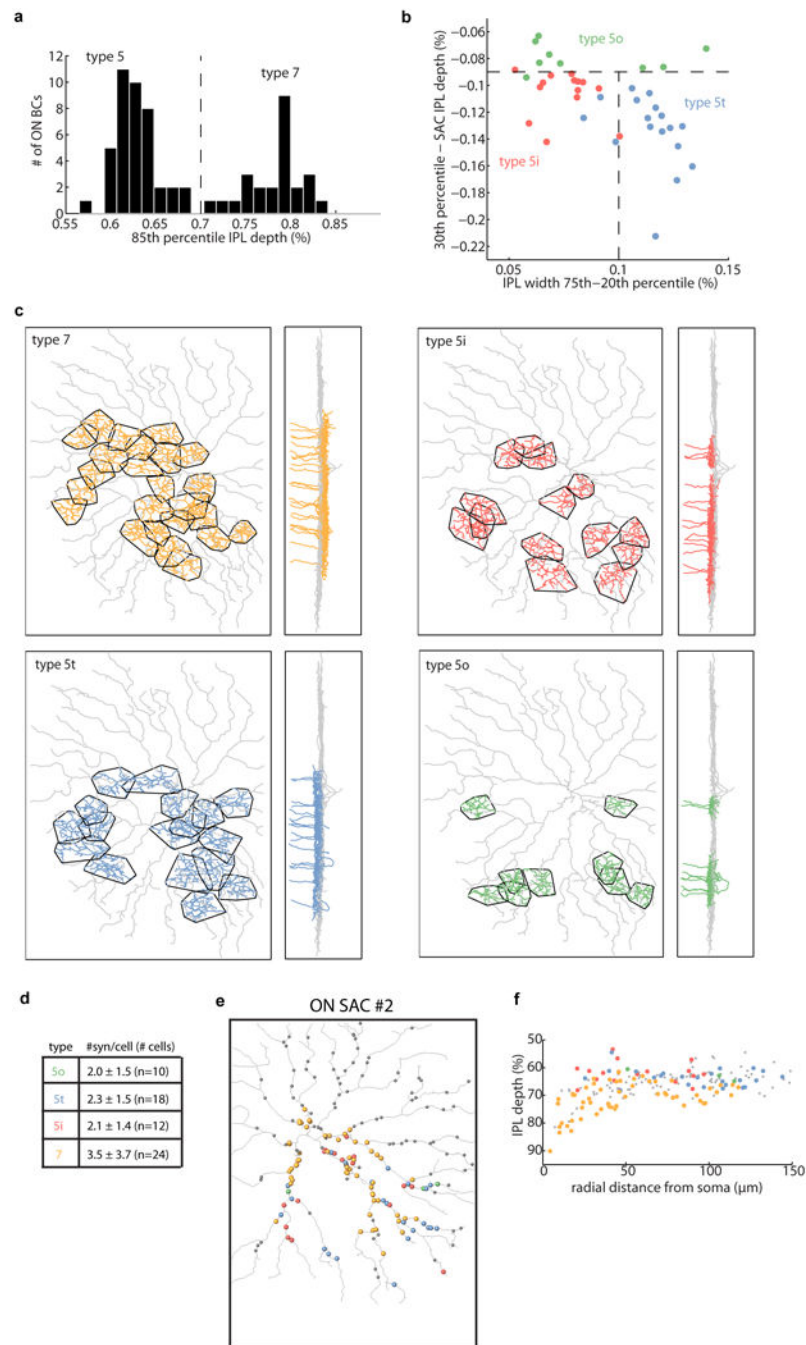
Extended Data
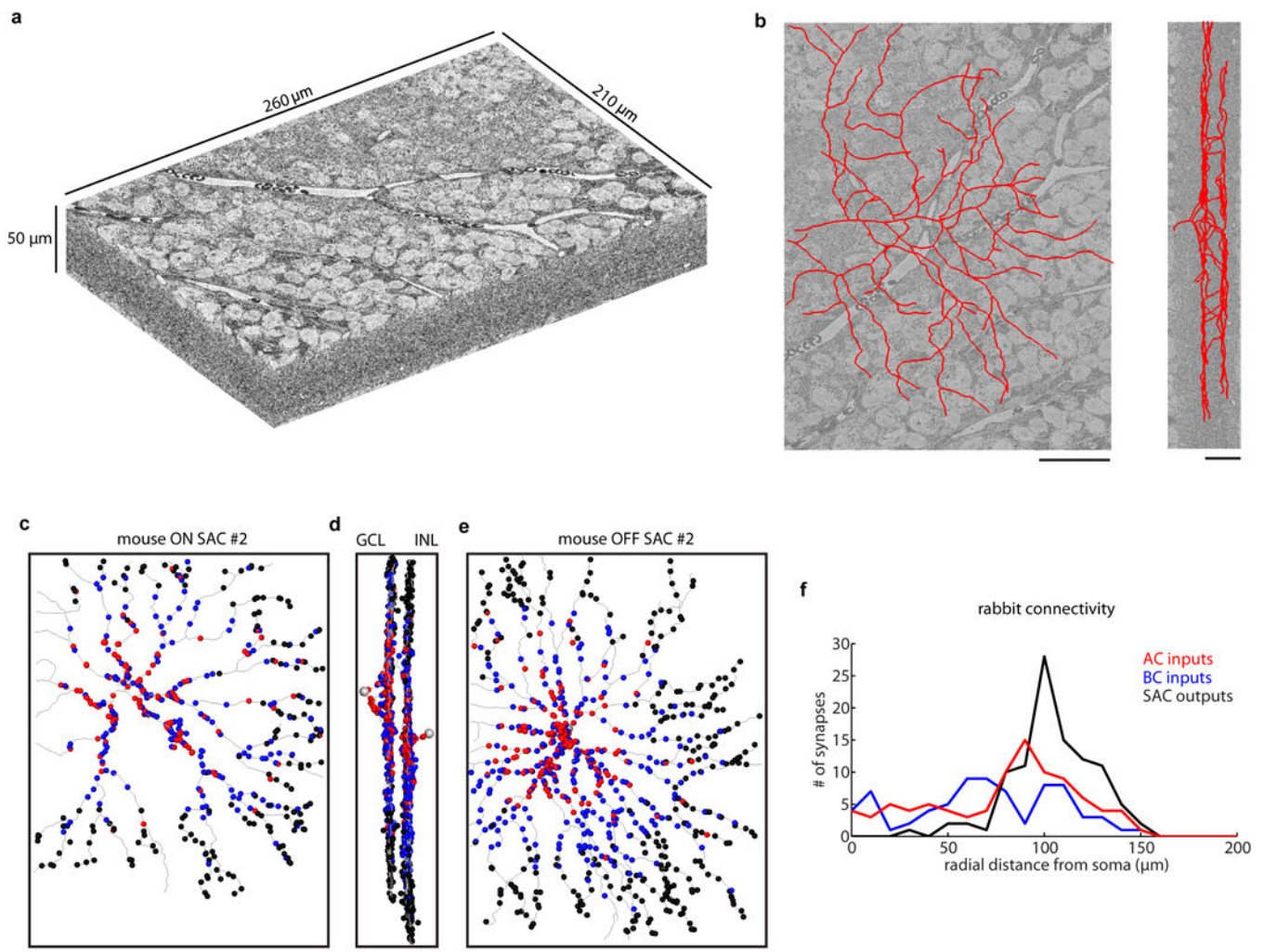
Extended Data Figure 1. EM dataset, additional SAC reconstructions and rabbit connectivity
a, Conventionally stained SBEM volume of a mouse retina. **b**, Reconstructed ON-OFF DSGC. **c–e**, A second reconstructed ON and OFF SAC with annotated synapses locations. **f**, Annotation of the radial distribution of input and output synapses to and from approximately one half of an OFF SAC dendritic arbor in rabbit retina. Data adapted from Famiglietti (1991), figure 15.
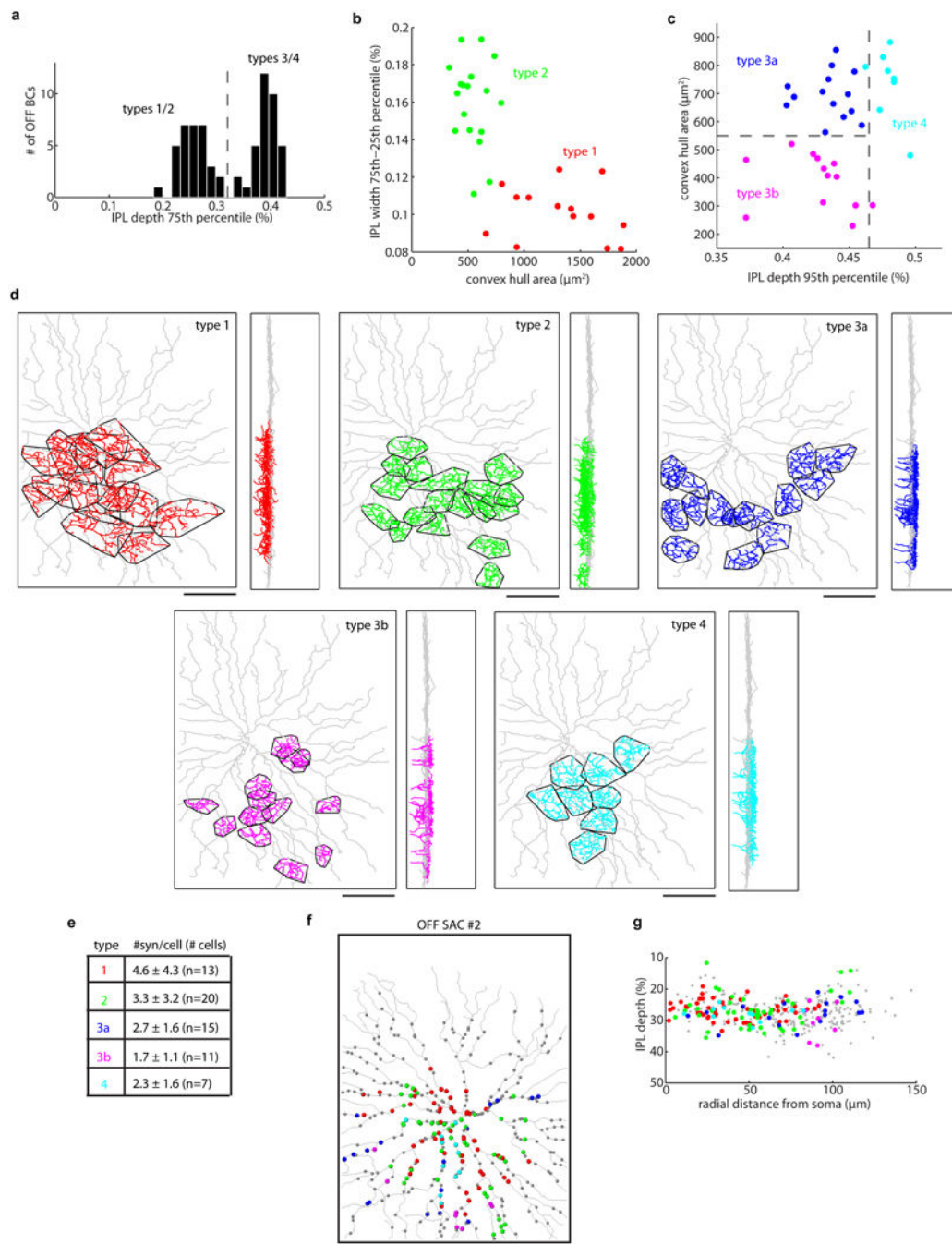
Extended Data Figure 2. Classification of OFF BCs
a, Types 1/2 and types 3/4 separated by IPL depth. **b**, Types 1 and 2 separate by stratification width and axonal arborization area (convex hull). **c**, Types 3a, 3b and 4 separate by stratification depth and axonal arborization area. **d**, Mosaic patterns and stratification profiles of OFF BCs. **e**, Summary table indicating the number of synapses (mean ± SD) each BC, by type, formed with each SAC. **f**, Location of BC synapses onto a second OFF SAC, color-coded by BC type. **g**, The IPL depth of each synapse versus the radial distance relative to the soma.

Extended Data Figure 3. Classification of ON BCs
a, Type 5 and type 7 BCs separated by IPL depth. **b**, Types 5o (outer), 5t (thick) and 5i (inner) further subdivide based on IPL depth and stratification width. **c**, Mosaic patterns and stratification profiles of ON BCs. **d**, Summary table indicating the number of synapses (mean ± SD) each BC, by type, formed with each SAC. **e**, Location of BC synapses onto a second ON SAC, color-coded by BC type. **f**, The IPL depth of each synapse versus the radial distance relative to the soma.
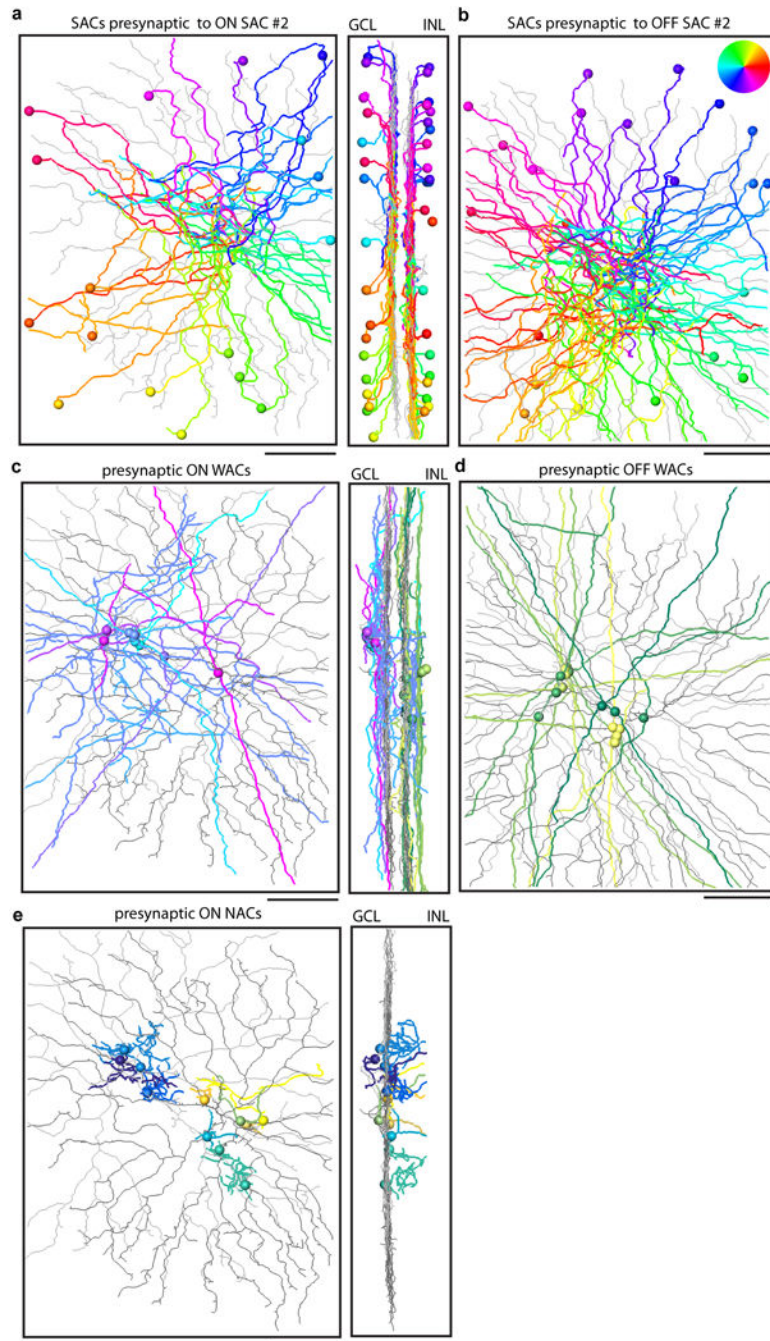
Extended Data Figure 4. Amacrine cell types presynaptic to SACs
a,b, SACs presynaptic to the second pair of mouse SACs color-coded by absolute orientation. **c,d**, WACs presynaptic to SACs. **e**, NACs presynaptic to ON SACs.
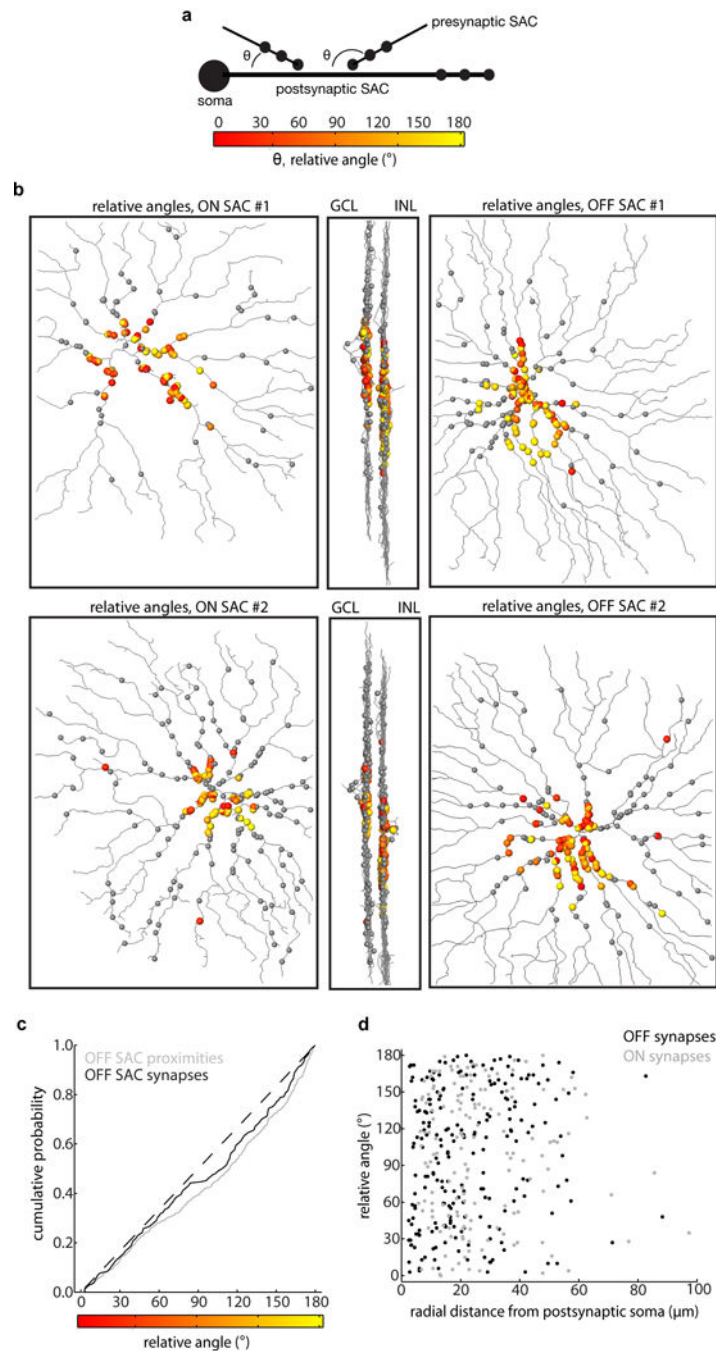
Extended Data Figure 5. Relative angles between presynaptic and postsynaptic SAC dendrites
a, Schematic of the relative angle measurement: parallel wiring = 0°, anti-parallel wiring = 180°. **b**, Locations of SAC input synapses color-coded by relative angle. Gray locations indicate AC synapses that were not analyzed. **c**, Cumulative distributions of the relative angles between each pre- and postsynaptic OFF SAC dendrite for synapses (black) and proximities (gray). Dashed line indicates a uniform distribution. **d**, Relative angle for each synapse was uncorrelated with the radial distance from the postsynaptic somas (r = 0.07, p = 0.16). Scale bar: 50 μm.
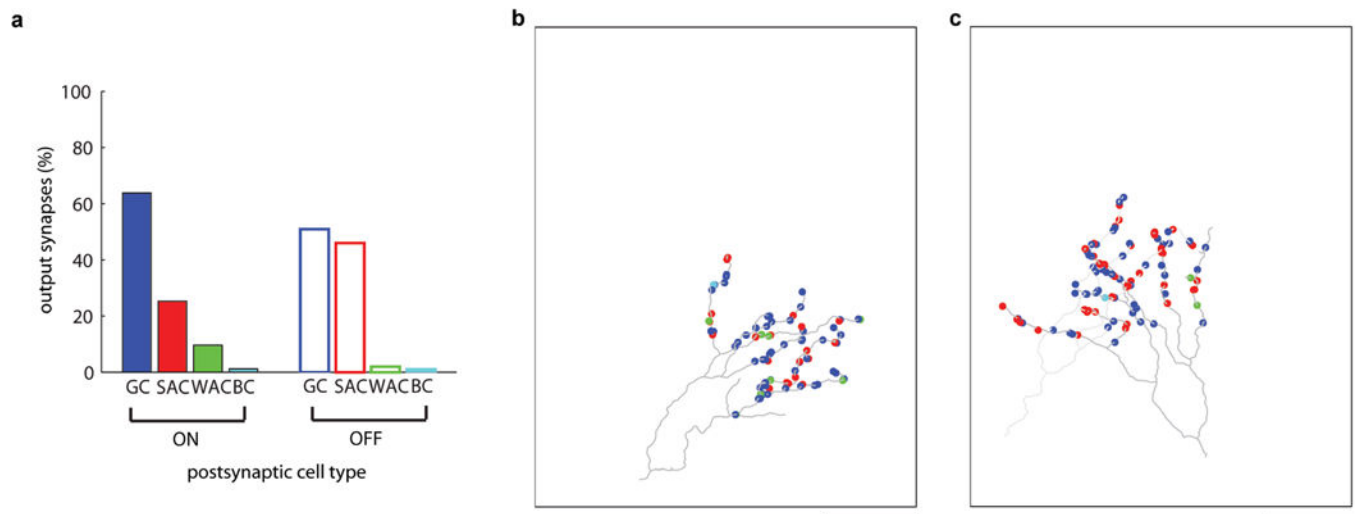
Extended Data Figure 6. Identities of neurons postsynaptic to SAC output synapses
a, Percentage of output synapses formed with different postsynaptic cell types, color-coded by postsynaptic cell class: GCs (blue), SACs (red), BCs (cyan), and WACs (green). **b**, Locations of 110 annotated output synapses on 2 OFF SAC dendrite fragments. **c**, Locations of 83 annotated output synapses on 1 ON SAC dendrite fragment. Scale bar = 50 μm.
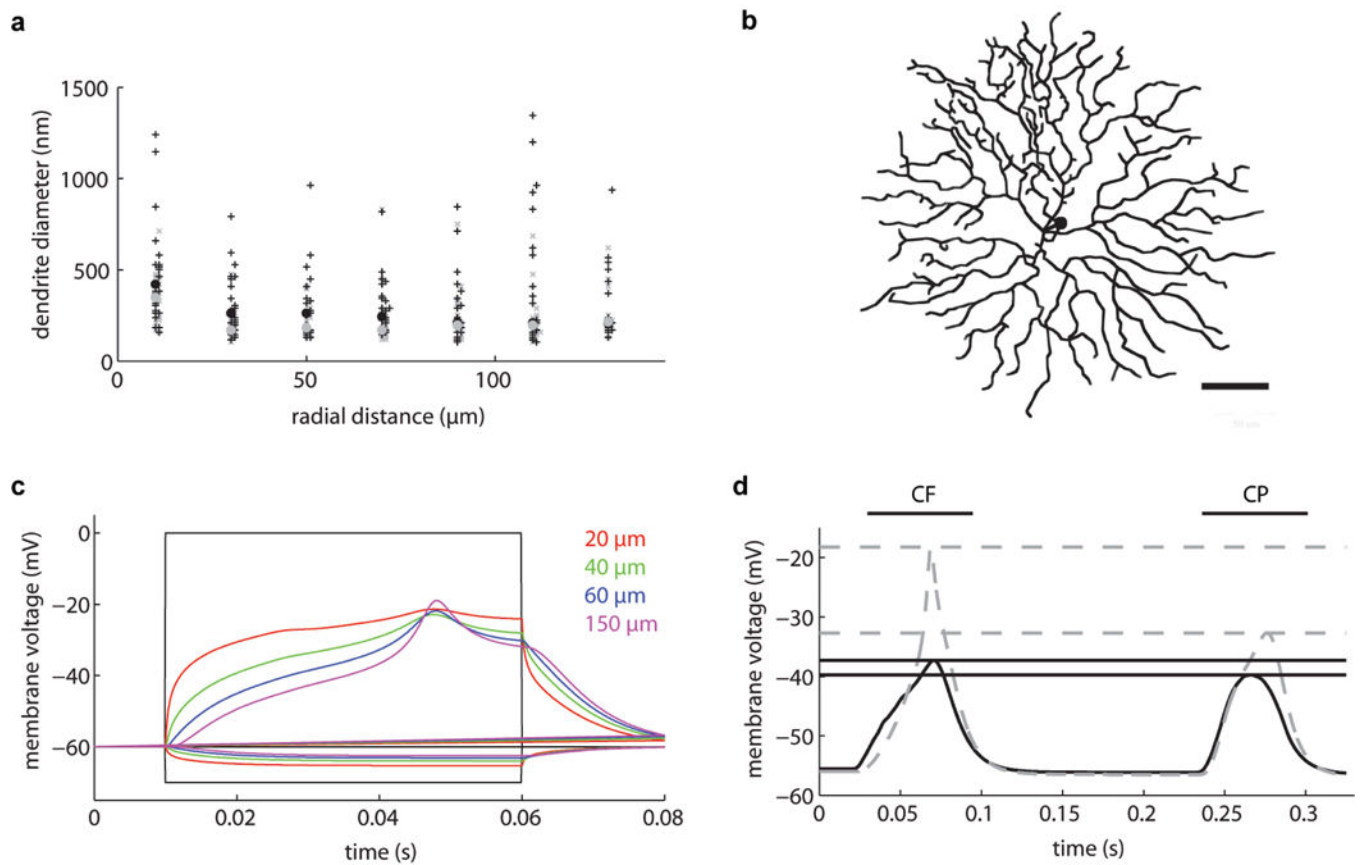
Extended Data Figure 7. Single SAC model

a, Dendrite diameters sampled from an ON SAC (gray) and an OFF SAC (black) at different radial distances from their respective somas. **b**, Single SAC morphology used in all simulations. **c**, Somatic voltage clamp simulation showed poor space clamp of even proximal dendrites. Voltage traces measured at a different distances (20 – 150 μm) from the soma. **d**, Somatic (solid line) and distal dendrite (dashed line) voltage time series in response to an annulus moving centrifugally (CF) or centripetally (CP). The addition of active conductances to SAC dendrites (see Extended Data Table 1) rendered somatic voltage recordings DS for CF compared to CP stimulation, in agreement with electrophysiological measurements. Scale bar = 50 μm.
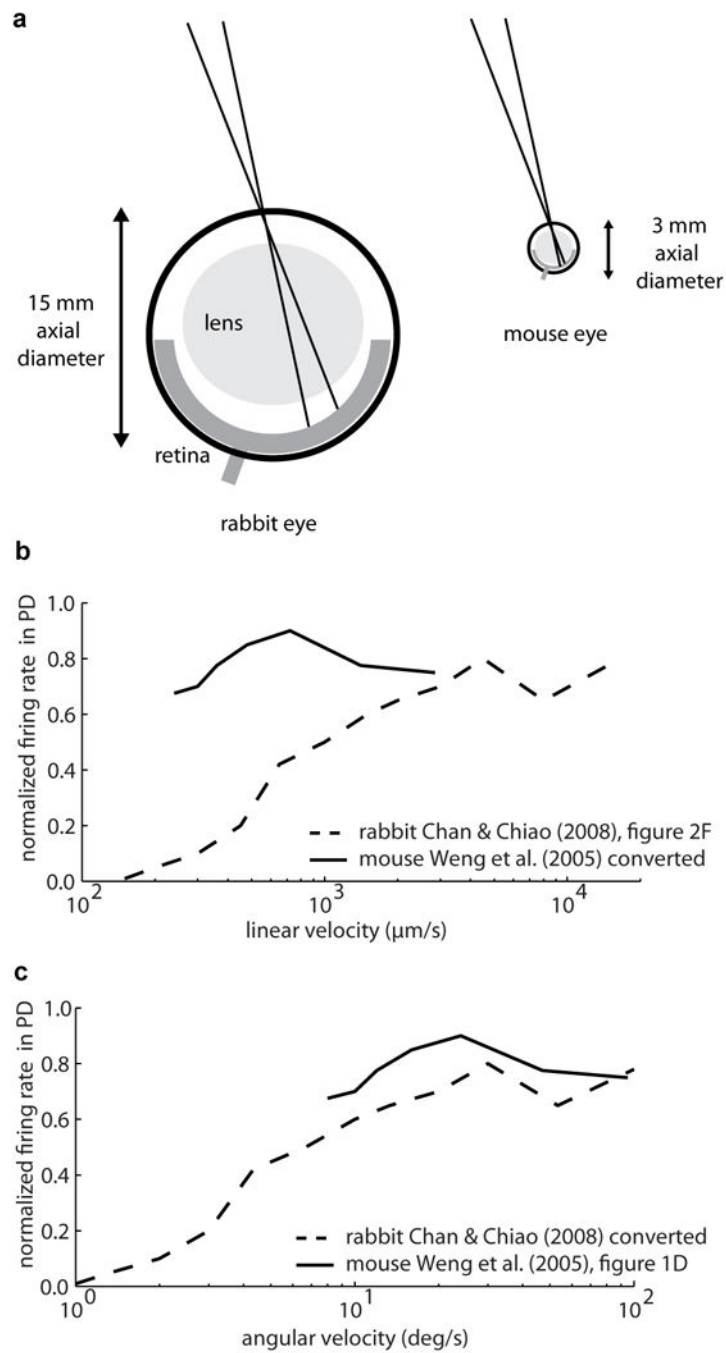
Extended Data Figure 8. Velocity tuning of rabbit and mouse DS circuits
a, Schematic of the difference in axial diameters and subtended angle on the retina of rabbit and mouse eyes. **b**, Linear velocity tuning curves from rabbit and mouse ON-OFF DSGCs. **c**, Angular velocity tuning curves from rabbit and mouse ON-OFF DSGCs. Data adapted from Chan & Chiao (2008), figure 2F and Weng et al (2005), figure 1D.

Extended Data Table 1

Table of biophysical parameters used in model SACs.

a Biophysical parameters for SAC model		
R_m (Ω-cnV)		10,000
R_i (Ω-cm^2)		75
NaV1.8 channel density (S/cm^2)	soma:	0
	proximal 1/3:	0
	medial 1/3:	3e^{-3}
	distal 1/3:	3e^{-3}
Kdr channel density (S/cm^2)	soma	3e^{-3}
	proximal 1/3:	2e^{-3}
	medial 1/3:	2e^{-3}
	distal 1/3:	2e^{-3}
L-type Ca2+ channel density (S/cm^2)	soma	0
	proximal 1/3:	0
	medial 1/3:	1e^{-3}
	distal 1/3:	1e^{-3}

Acknowledgments

References

1. Barlow HB, Hill RM, Levick WR. Retinal Ganglion Cells Responding Selectively to Direction and Speed of Image Motion in the Rabbit. J Physiol. 1964; 173:377–407. [PubMed: 14220259]

2. Famiglietti EV. Synaptic organization of starburst amacrine cells in rabbit retina: analysis of serial thin sections by electron microscopy and graphic reconstruction. The Journal of comparative neurology. 1991; 309:40–70. DOI: 10.1002/cne.903090105 [PubMed: 1894768]

3. Vaney, DI.; Collin, SP.; Young, HM. Neurobiology of the inner retina. Weiler, R.; Osborne, NN., editors. Springer; 1989. p. 157-168.

4. Briggman KL, Helmstaedter M, Denk W. Wiring specificity in the direction-selectivity circuit of the retina. Nature. 2011; 471:183–188. DOI: 10.1038/nature09818 [PubMed: 21390125]

5. Wei W, Hamby AM, Zhou K, Feller MB. Development of asymmetric inhibition underlying direction selectivity in the retina. Nature. 2011; 469:402–406. DOI: 10.1038/nature09600 [PubMed: 21131947]

6. Hausselt SE, Euler T, Detwiler PB, Denk W. A dendrite-autonomous mechanism for direction selectivity in retinal starburst amacrine cells. PLoS biology. 2007; 5:e185. [PubMed: 17622194]

7. Euler T, Detwiler PB, Denk W. Directionally selective calcium signals in dendrites of starburst amacrine cells. Nature. 2002; 418:845–852. DOI: 10.1038/nature00931 [PubMed: 12192402]

8. Lee S, Zhou ZJ. The synaptic mechanism of direction selectivity in distal processes of starburst amacrine cells. Neuron. 2006; 51:787–799. DOI: 10.1016/j.neuron.2006.08.007 [PubMed: 16982423]

9. Tukker JJ, Taylor WR, Smith RG. Direction selectivity in a model of the starburst amacrine cell. Vis Neurosci. 2004; 21:611–625. DOI: 10.1017/s0952523804214109 [PubMed: 15579224]

10. Gavrikov KE, Dmitriev AV, Keyser KT, Mangel SC. Cation–chloride cotransporters mediate neural computation in the retina. Proceedings of the National Academy of Sciences of the United States of America. 2003; 100:16047–16052. DOI: 10.1073/pnas.2637041100 [PubMed: 14665697]

11. Oesch NW, Taylor WR. Tetrodotoxin-resistant sodium channels contribute to directional responses in starburst amacrine cells. PloS one. 2010; 5:e12447. [PubMed: 20805982]

12. Kim JS, et al. Space-time wiring specificity supports direction selectivity in the retina. Nature. 2014; 509:331–336. DOI: 10.1038/nature13240 [PubMed: 24805243]

13. Taylor WR, Smith RG. The role of starburst amacrine cells in visual signal processing. Visual Neuroscience. 2012; 29:73–81. DOI: 10.1017/s0952523811000393 [PubMed: 22310373]

14. Munch TA, Werblin FS. Symmetric interactions within a homogeneous starburst cell network can lead to robust asymmetries in dendrites of starburst amacrine cells. Journal of neurophysiology. 2006; 96:471–477. DOI: 10.1152/jn.00628.2005 [PubMed: 16598066]

15. Enciso GA, et al. A model of direction selectivity in the starburst amacrine cell network. Journal of computational neuroscience. 2010; 28:567–578. DOI: 10.1007/s10827-010-0238-3 [PubMed: 20524107]

16. Millar TJ, Morgan IG. Cholinergic amacrine cells in the rabbit retina synapse onto other cholinergic amacrine cells. Neuroscience letters. 1987; 74:281–285. [PubMed: 3550530]

17. Denk W, Horstmann H. Serial block-face scanning electron microscopy to reconstruct three-dimensional tissue nanostructure. PLoS biology. 2004; 2:e329. [PubMed: 15514700]

18. Dacheux RF, Chimento MF, Amthor FR. Synaptic input to the on-off directionally selective ganglion cell in the rabbit retina. The Journal of comparative neurology. 2003; 456:267–278. DOI: 10.1002/cne.10521 [PubMed: 12528191]

19. Roska B, Werblin F. Vertical interactions across ten parallel, stacked representations in the mammalian retina. Nature. 2001; 410:583–587. DOI: 10.1038/35069068 [PubMed: 11279496]

20. Baden T, Berens P, Bethge M, Euler T. Spikes in mammalian bipolar cells support temporal layering of the inner retina. Current biology : CB. 2013; 23:48–52. DOI: 10.1016/j.cub.2012.11.006 [PubMed: 23246403]

21. Borghuis BG, Marvin JS, Looger LL, Demb JB. Two-photon imaging of nonlinear glutamate release dynamics at bipolar cell synapses in the mouse retina. The Journal of neuroscience : the official journal of the Society for Neuroscience. 2013; 33:10972–10985. DOI: 10.1523/jneurosci.1241-13.2013 [PubMed: 23825403]

22. Greene MJ, Kim JS, Seung HS, EyeWirers. Analogous Convergence of Sustained and Transient Inputs in Parallel On and Off Pathways for Retinal Motion Computation. Cell reports. 2016; 14:1892–1900. DOI: 10.1016/j.celrep.2016.02.001 [PubMed: 26904938]

23. Ichinose T, Fyk-Kolodziej B, Cohn J. Roles of ON cone bipolar cell subtypes in temporal coding in the mouse retina. The Journal of neuroscience : the official journal of the Society for Neuroscience. 2014; 34:8761–8771. DOI: 10.1523/JNEUROSCI.3965-13.2014 [PubMed: 24966376]

24. Hoggarth A, et al. Specific wiring of distinct amacrine cells in the directionally selective retinal circuit permits independent coding of direction and size. Neuron. 2015; 86:276–291. DOI: 10.1016/j.neuron.2015.02.035 [PubMed: 25801705]

25. Ishii T, Kaneda M. ON-pathway-dominant glycinergic regulation of cholinergic amacrine cells in the mouse retina. The Journal of Physiology. 2014; 592:4235–4245. DOI: 10.1113/jphysiol.2014.271148 [PubMed: 25085888]

26. Park SJH, Kim IJ, Looger LL, Demb JB, Borghuis BG. Excitatory Synaptic Inputs to Mouse On-Off Direction-Selective Retinal Ganglion Cells Lack Direction Tuning. The Journal of Neuroscience. 2014; 34:3976–3981. DOI: 10.1523/jneurosci.5017-13.2014 [PubMed: 24623775]

27. Yonehara K, et al. The first stage of cardinal direction selectivity is localized to the dendrites of retinal ganglion cells. Neuron. 2013; 79:1078–1085. DOI: 10.1016/j.neuron.2013.08.005 [PubMed: 23973208]

28. Chen M, Lee S, Park SJ, Looger LL, Zhou ZJ. Receptive field properties of bipolar cell axon terminals in direction-selective sublaminas of the mouse retina. Journal of neurophysiology. 2014; 112:1950–1962. DOI: 10.1152/jn.00283.2014 [PubMed: 25031256]

29. Bozkir G, Bozkir M, Dogan H, Aycan K, Guler B. Measurements of axial length and radius of corneal curvature in the rabbit eye. Acta medica Okayama. 1997; 51:9–11. [PubMed: 9057929]

30. Park H, et al. Assessment of axial length measurements in mouse eyes. Optometry and vision science : official publication of the American Academy of Optometry. 2012; 89:296–303. DOI: 10.1097/OPX.0b013e31824529e5 [PubMed: 22246334]

31. Chan YC, Chiao CC. Effect of visual experience on the maturation of ON-OFF direction selective ganglion cells in the rabbit retina. Vision research. 2008; 48:2466–2475. DOI: 10.1016/j.visres.2008.08.010 [PubMed: 18782584]

32. Weng S, Sun W, He S. Identification of ON-OFF direction-selective ganglion cells in the mouse retina. J Physiol. 2005; 562:915–923. DOI: 10.1113/jphysiol.2004.076695 [PubMed: 15564281]

33. Denk W, Strickler JH, Webb WW. Two-photon laser scanning fluorescence microscopy. Science. 1990; 248:73–76. [PubMed: 2321027]

34. Euler T, et al. Eyecup scope–optical recordings of light stimulus-evoked fluorescence signals in the retina. Pflugers Archiv : European journal of physiology. 2009; 457:1393–1414. DOI: 10.1007/s00424-008-0603-5 [PubMed: 19023590]

35. Grzywacz NM, Amthor FR. Robust directional computation in on-off directionally selective ganglion cells of rabbit retina. Visual Neuroscience. 2007; 24:647–661. [PubMed: 17900380]

36. Morgan JL, Lichtman JW. Why not connectomics? Nature methods. 2013; 10:494–500. DOI: 10.1038/nmeth.2480 [PubMed: 23722208]

37. Denk W, Briggman KL, Helmstaedter M. Structural neurobiology: missing link to a mechanistic understanding of neural computation. Nat Rev Neurosci. 2012; 13:351–358. DOI: 10.1038/nrn3169 [PubMed: 22353782]

38. Vlasits AL, et al. A Role for Synaptic Input Distribution in a Dendritic Computation of Motion Direction in the Retina. Neuron. 2016; 89:1317–1330. DOI: 10.1016/j.neuron.2016.02.020 [PubMed: 26985724]

39. Vaney DI. 'Coronate' amacrine cells in the rabbit retina have the 'starburst' dendritic morphology. Proceedings of the Royal Society of London. Series B, Biological sciences. 1984; 220:501–508.

40. Tauchi M, Masland RH. The shape and arrangement of the cholinergic neurons in the rabbit retina. Proceedings of the Royal Society of London. Series B, Biological sciences. 1984; 223:101–119.

41. Perez De Sevilla Muller L, Shelley J, Weiler R. Displaced amacrine cells of the mouse retina. The Journal of comparative neurology. 2007; 505:177–189. DOI: 10.1002/cne.21487 [PubMed: 17853452]

42. Keeley PW, Whitney IE, Raven MA, Reese BE. Dendritic spread and functional coverage of starburst amacrine cells. The Journal of comparative neurology. 2007; 505:539–546. DOI: 10.1002/cne.21518 [PubMed: 17924572]

43. Kostadinov D, Sanes JR. Protocadherin-dependent dendritic self-avoidance regulates neural connectivity and circuit function. eLife. 2015; 4

44. Helmstaedter M, et al. Connectomic reconstruction of the inner plexiform layer in the mouse retina. Nature. 2013; 500:168–174. DOI: 10.1038/nature12346 [PubMed: 23925239]

45. Smith RG. NeuronC: a computational language for investigating functional architecture of neural circuits. Journal of neuroscience methods. 1992; 43:83–108. [PubMed: 1405746]

46. Schachter MJ, Oesch N, Smith RG, Taylor WR. Dendritic spikes amplify the synaptic signal to enhance detection of motion in a simulation of the direction-selective ganglion cell. PLoS computational biology. 2010; 6

47. Pologruto TA, Sabatini BL, Svoboda K. ScanImage: flexible software for operating laser scanning microscopes. Biomedical engineering online. 2003; 2:13. [PubMed: 12801419]
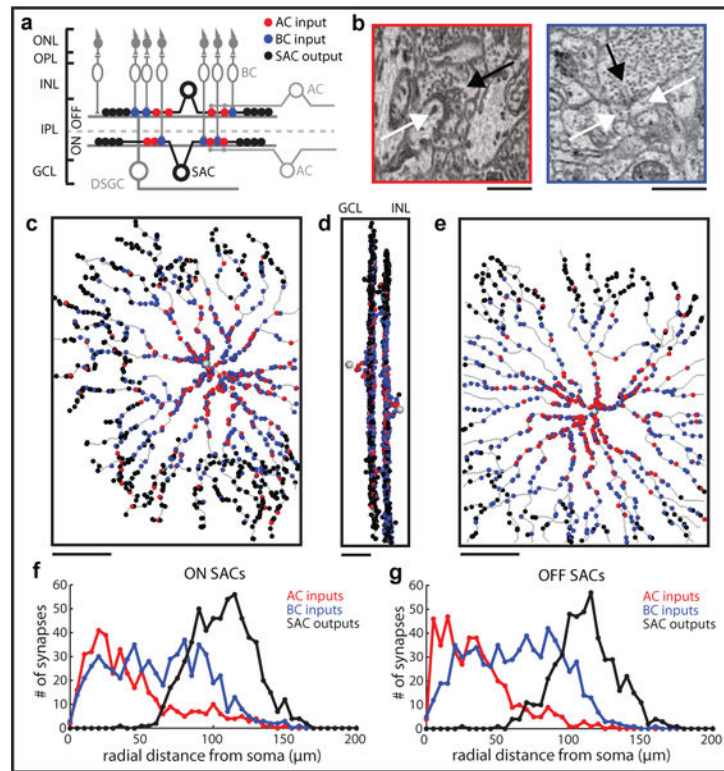
Figure 1. Synaptic connectivity of mouse SACs
a, Schematic diagram of DS circuitry. **b**, Representative examples of a presynaptic SAC (black arrow, left) contacting a postsynaptic SAC (white arrow, left) and a presynaptic BC (black arrow, right) forming a ribbon synapse with two postsynaptic SACs (white arrows, right). **c,e**, Distribution of excitatory (blue) and inhibitory (red) input synapses and output synapses (black) onto ON and OFF SACs. **d**, Horizontal view of ON and OFF SACs, whose somata reside in the ganglion cell layer (GCL) or inner nuclear layer (INL), respectively. **f,g**, Histograms of radial distances from the soma for annotated synapses. Data pooled from n = 2 ON and n = 2 OFF SACs. Scale bars: 1 μm (**b**), 50 μm (**c,e**), 25 μm (**d**).
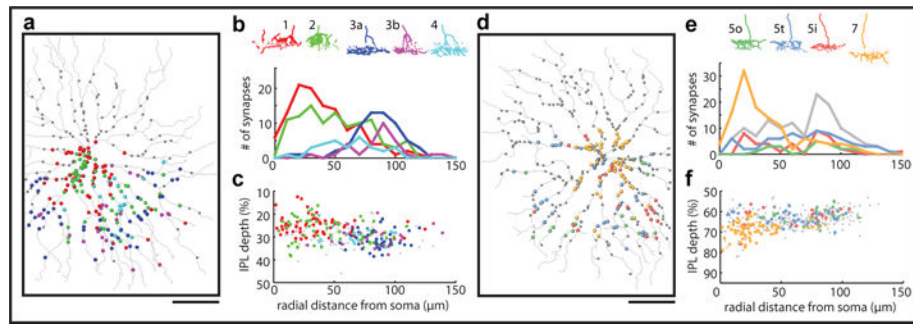
Figure 2. BC inputs to mouse SACs

a, Location of BC synapses onto an OFF, color-coded by BC type (**b**). Gray dots indicate BC synapses that were not analyzed. **b**, Total OFF BC synapses (n = 343) onto n = 2 OFF SACs versus radial distance from soma. **c**, IPL depth of each synapse versus the radial distance relative to their soma. **d–f**, As in **a–c** for ON SACs, (n = 262) ON BC synapses onto n = 2 ON SACs. Gray line (**e**) indicates pooled inputs from all three type 5 BCs. Scale bar: 50 μm.
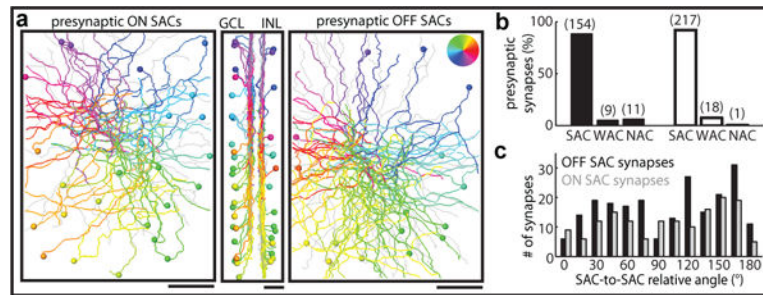
Figure 3. Inhibitory inputs to mouse SACs
a, SAC dendrites presynaptic to an ON and OFF SAC, color-coded by absolute orientation. 33% (n = 30) of OFF dendrites and 45% (n = 30) of ON dendrites traced back to somas within the dataset, corresponding to inter-soma distances between connected SACs of 98.5 ± 35.9 µm (OFF, mean ± SD) and 113.4 ± 37.0 µm (ON, mean ± SD), consistent with the spacing of connected SACs based on paired recordings in adult mice[43]. **b**, Input synapses originating from different amacrine cells. **c**, Histogram of relative angle (θ) between each pre- and postsynaptic SAC dendrite for OFF (n = 217, black) and ON (n = 154, gray) SACs. Scale bar: 50 µm.

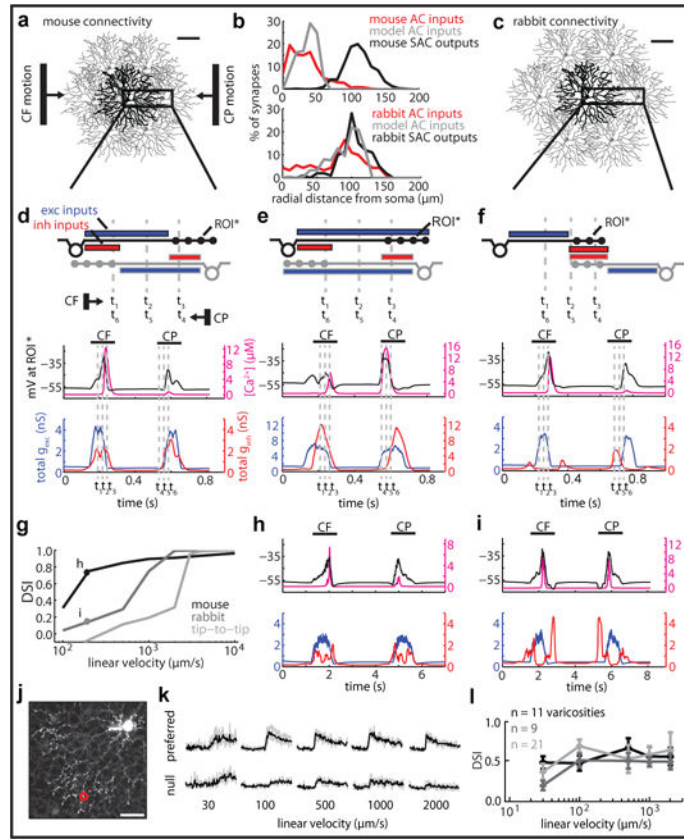**Figure 4. Functional consequences of SAC network connectivity**

Compartmental models of mouse (**a**) and rabbit (**c**) networks. **b**, Radial distributions of simulated synapses compared to anatomical reconstructions (rabbit data adapted from ref. 2). **d**, Schematic of mouse connectivity (top) and simulated responses (bottom) to CF and CP bar stimuli relative to location ROI*. Bar location at times $t_1 - t_6$ indicated by dashed gray lines. Voltage and calcium responses measured at ROI*; synaptic conductances measured for the central SAC. **e**, As in **d**, but with BC inputs distributed uniformly along SAC dendrites. **f**, As in **d**, but incorporating rabbit-like connectivity. **g**, Simulated velocity tuning curves. DSI calculated from $[Ca^{2+}]$ at ROI*. **h,i**, Simulated responses at 200 μm/s for mouse and rabbit models, respectively. **j**, Fluorescence image of an ON SAC filled with OGB1. **k**, Representative Ca^{2+} transients measured at the varicosity highlighted in **j** in response to visual stimuli moving at 5 different velocities (300% contrast). **l**, Velocity tuning of DSI (mean ± SD) in n = 41 SAC varicosities measured from n = 3 ON SACs. Scale bars: 100 μm (**a,c**), 25 μm (**j**).
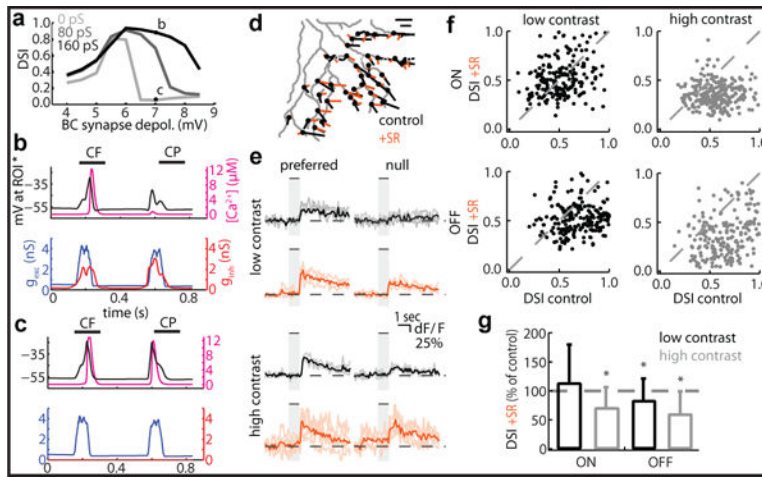
Figure 5. Contrast dependence of SAC to SAC inhibition

a–c, Contrast tuning curve of mouse network model (light bar stimulus). Increasing contrast was simulated with stronger BC depolarization. The maximal conductance of inhibitory synapses in the model was varied. **d**, Directional tuning of individual SAC varicosities. Vectors indicate preferred direction and DSI magnitude. Scale bars: 10 μm (upper), 0.5 DSI (lower). **e**, Representative Ca^{2+} transients from individual varicosities under low (100%) and high (300%) contrast (SR: SR95531). **f**, DSI of individual varicosities for ON (left: n = 201 ROIs from n = 6 cells; right: n = 261 ROIs from n = 10 cells) and OFF (left: n = 193 ROIs from n = 4 cells; right: n = 197 ROIs from n = 9 cells) SACs. **g**, DSI (mean ± SD) following SR application as a fraction of control (paired t-test, Bonferroni correction, * = p < 0.001).
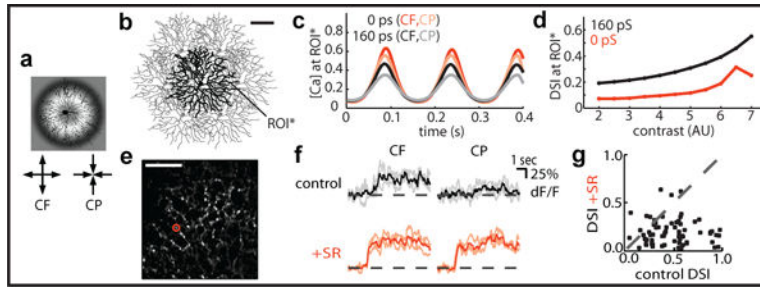
Figure 6. Receptive field structure of mouse SACs

The mouse network model (**b**) was activated with a bullseye stimulus (**a**) centered on and restricted to the diameter of the central SAC and expanded or contracted to elicit CF or CP motion. **c**, Simulated dendritic $[Ca^{2+}]$ at ROI* in response to CF and CP bullseyes (6.7 Hz, 150 μm period, 0.05 AU contrast) with inhibition intact (black/gray) or blocked (orange/peach). **d**, DSI versus simulated contrast. **e**, Fluorescence image of OGB1-filled SAC. **f**, Representative dendritic Ca^{2+} transients recorded in response to CF and CP bullseye stimuli (2 Hz, 140 μm period, 90% contrast). Responses from the ROI in **e**. **g**, Scatter plot of n = 74 ROIs from n = 5 ON SACs. SR95531 application significantly decreased DSI from 0.46 ± 0.24 (mean ± SD) to 0.17 ± 0.14 (paired t-test, p = 2×10^{-13}). Scale bars: 100 μm (**b**), 25 μm (**e**).